



Lab on a Chip

Kinetic analysis of the growth behavior of perovskite CsPbBr₃ nanocrystals in a microfluidic system

Journal:	<i>Lab on a Chip</i>
Manuscript ID	LC-ART-04-2022-000331.R1
Article Type:	Paper
Date Submitted by the Author:	20-Jun-2022
Complete List of Authors:	Tang, Xiaobing; University of Kentucky, Chemical and Materials Engineering Yang, Fuqian; University of Kentucky, Chemical and Materials Engineering

SCHOLARONE™
Manuscripts

Kinetic analysis of the growth behavior of perovskite CsPbBr₃ nanocrystals
in a microfluidic system

Xiaobing Tang and Fuqian Yang*

Materials Program, Department of Chemical and Materials Engineering, University of
Kentucky, Lexington, KY 40506, USA

*Corresponding author. E-mail: fuqian.yang@uky.edu (F. Yang)

Abstract

Understanding the growth behavior of nanoparticles and semiconductor nanocrystals under dynamic environments is of profound importance in controlling the sizes and uniformity of the prepared nanoparticles and semiconductor nanocrystals. In this work, we develop a relation between the bandgap (the photoluminescence peak wavelength) of semiconductor nanocrystals and the total flow rate for the synthesis of the semiconductor nanocrystals in microfluidic systems under the framework of quantum confinement effect without contribution of Coulomb interaction. Using the relation, we analyze the growth behavior of the CsPbBr₃ nanocrystals synthesized in a microfluidic system by an antisolvent method in a temperature range of 303 to 363 K. The results demonstrate that the square of the average size of the CsPbBr₃ nanocrystals is inversely proportional to total flow rate and support the developed relation. The activation energy for the rate process controlling the growth of the CsPbBr₃ nanocrystals in the microfluidic system is 2.05 kJ/mol. Increasing the synthesis temperature widens the size distribution of the CsPbBr₃ NCs prepared in the microfluidic system. The method developed in this work provides a simple approach to use photoluminescent characteristics to in-situ monitor and analyze the growth of semiconductor nanocrystals under dynamic environments.

Keywords: Microfluidics; CsPbBr₃ nanocrystals; kinetics; Flow rate; Temperature.

Introduction

Microfluidics, derived originally from microelectronic fabrication processes and microelectromechanical devices and systems, is an active research field for Lab-on-Chip technology and has become an important technique in bioengineering, chemical analysis, optoelectronics and other fields. Microfluidic-based chips have been used in applications of medical diagnostics¹⁻³, biological detection⁴, optoelectronic monitoring^{5, 6}, three-dimensional printing⁷⁻⁹, synthesis of nanoparticles^{10, 11} and so forth, attributed to a wide range of their merits including low cost, high sensitivity, less reagent consumption, etc.

Semiconductor nanocrystals (NCs), also referred to as quantum dots (QDs), which exhibit quantum confinement effect for their characteristic dimensions being comparable to (or smaller than) the exciton Bohr radius¹² or electrons being constrained to a domain comparable to their de Broglie wavelength¹³, have a variety of applications in optoelectronics including lighting emitting diodes (LEDs), solar cells, liquid crystals display (LCD), etc.^{13,14} Over the past decades, there have been extensive studies on the synthesis and applications of cadmium (Cd)-based chalcogenides NCs. However, the costly and complex synthesis processes for core-shell NCs of high stabilities have hindered their industrialization and commercialization. On the other side, lead halide perovskite nanocrystals (PeNCs) with lower cost and more facile synthesis processes than conventional Cd-based chalcogenides NCs have attracted wide interest for applications in solar cells^{15, 16} and have been considered as potential materials for next-generation high-performance lighting and display due to their huge merits of high color purity, high brightness, high defect tolerance and so forth.^{14,17,18} Additionally, all-inorganic (commonly Cs-based) PeNCs are more promising than organic-inorganic hybrid (commonly CH_3NH_3 (MA) or $\text{CH}(\text{NH}_2)_2$ (FA)-based) PeNCs in optoelectronic applications due to their higher chemical stability.^{19, 20}

There are reports on the use of microfluidic systems to synthesize all-inorganic PeNCs.²¹⁻²³ Microfluidics provides a high-efficient, reproducible and continuous route for the synthesis of PeNCs and outperforms conventional batch-mode methods of small amount, which suffers from the issues associated with the size control and distribution from batch to batch.²⁴ Compared with the conventional small batch-mode methods for fundamental

research, microfluidics is an efficient methods for large-scale preparation of PeNCs.²⁴ Microfluidic synthesis also possesses the merits of easy temperature control, large heat and mass transfer, efficient mixing, etc.²⁵ Using an automated microfluidic platform, Epps et al.²⁶ were able to synthesize CsPbBr₃ QDs. Lignos et al.²⁷ synthesized CsPbX₃ (X = Br, I, Cl, Cl/Br and Br/I) NCs via a droplet-based microfluidic platform and studied the effects of the molar ratios of Pb to Cs and I to Br, temperature and reaction time on the photoluminescence (PL) emission of the as-obtained perovskite NCs. Incorporating NCs in polymers with a microfluidic-spinning microreactor, Ma et al.²⁸ produced poly(methyl)methacrylate (PMMA)-CsPbBr₃ nanocomposites and studied fluorescence of the nanocomposites with the focus on optoelectronic applications, including LED, microfibers and LCD. Zhang et al.²³ observed five different cross-sections of the all-inorganic PeNCs prepared in a PTFE-based microfluidic system. Applying artificial intelligence in the analysis of the synthesis of CsPbBr₃ QDs in a three-phase microfluidic platform, Abolhasani et al.²⁹ performed closed-loop formulation optimization and were able to improve the continuous manufacturing. Li et al.³⁰ investigated the dependence of the PL characteristics on reaction temperature, ligand, and alkyl-chain structure of the ligand. Geng et al.³¹ demonstrated the effects of residence time on the evolutions of the morphology and grain sizes of the CsPbBr₃ NCs synthesized in a microfluidic system. Guo et al.³² prepared CsPbI₃-mesoporous SiO₂ nanocomposites via a microfluidic system made from polytetrafluoroethylene (PTFE) capillary. They did not provide any information about the synthesis temperatures. Bao et al.³³ prepared Cs₄PbBr₆ perovskite microcrystals in a microfluidic system at 150 °C. Note that all the above studies required a high temperature around 400 K in the synthesis of the PeNCs for a variety of applications of microfibers,^{34, 35} lasers,²¹ and barcodes.³⁶

Recently, Abdel-Latif et al.³⁷ proposed a halide exchange apparatus for the room-temperature synthesis of Cs-based inorganic perovskite QDs of various emission wavelengths, which involves anion exchanges, in a microfluidic system. However, the preparation of the materials was so complicated and involved an oil-bath process at 433 K and evaporation at 393 K. Kang et al.³⁸ used halide exchange to synthesize CsPb(X/Y)₃ (X = Br, Y = Cl, I) NCs which exhibited light emission of 410-630 nm in the emission

wavelength. Maceiczky et al.³⁹ evaluated the effect of growth time on the size distribution of CdSe NCs synthesized in a microfluidics platform. Epps et al.²⁶ and Tang et al.⁴⁰ reported the effect of growth time on wavelength of CsPbBr₃ NCs. Zhang et al.⁴¹ demonstrated the morphological evolution of CsPbBr₃ NCs in a temperature of 50 – 120 °C.

In addition to all-inorganic CsPbX₃ NCs, organic-inorganic hybrid perovskite NCs have also been synthesized by microfluidics. Maceiczky et al.⁴² prepared FAPbX₃ (X = Br, I) NCs and tuned the emission wavelength by controlling ratio of Br to I and temperature. Lignos et al. fabricated FAPbX₃ (X = Cl, Br) NCs⁴³ with the emission wavelength in a range of 440-515 nm by changing the percentage of halide (Cl) element and Cs_xFA_{1-x}Pb(Br_{1-y}I_y)₃ NCs⁴⁴ with the emission wavelength in a range of 700-800 nm by adding Br ions and the emission wavelength in a range of 690-780 nm by controlling ratios of FA to Pb and Cs to Pb. Bezinge et al.⁴⁵ prepared (Cs/FA)Pb(I/Br)₃ and (Rb/Cs/FA)Pb(I/Br)₃ NCs with a self-optimizing algorithm in controlling the synthesis of the NCs with defined characteristics in the light emission

Understanding the growth kinetics/behavior of semiconductor NCs is critically important in controllable synthesis of semiconductor NCs. Yang⁴⁶ proposed a simple relation correlating the PL (photoluminescence) peak wavelength to the growth time without electrostatic interaction, which is supported by the experimental data for the growth of CdSe and CdSe/ZnS NCs given by Karim et al.⁴⁷ However, few studies have been focused on the growth behavior of PeNCs in microfluidic systems/microreactors. The understanding of the growth of PeNCs in microfluidic systems/microreactors remains elusive. There is a great need to develop a feasible method to study the growth behavior of PeNCs in microfluidic systems in order to control and optimize the synthesis of PeNCs.

Li et al.⁴⁸ reported an antisolvent method for the synthesis of PeNCs at room temperature. The formation of PeNCs in the antisolvent method is based on a reprecipitation process when an antisolvent (nonpolar or poor solvent) is added into the precursor solution prepared with a polar (good) solvent, due to much smaller solubility of ions in the antisolvent than in the precursor solution.^{18, 48} Such an approach is energy-saving and has potential of being integrated in microfluidic systems. Using an antisolvent approach in a three-phase

microfluidic system, Wei et al.⁴⁹ synthesized CsPbBr₃ NCs and studied the effect of the velocity ratios of different phases on the crystallinity and size of the NCs. Lin et al.⁵⁰ fabricated Ce³⁺-doped CsPbBr₃ NCs and tuned the doping concentration by the flow rate. Ng et al.⁵¹ investigated the effect of precursor mixing rate on the synthesis of CsPbBr₃ NCs by an antisolvent approach in a microfluidic platform. Few works have assessed the growth behavior of PeNCs synthesized in microfluidic systems. The purpose of this work is to analyze the growth behavior of the CsPbBr₃ NCs prepared by an antisolvent method in a microfluidic system by evaluating the dependences of the PL characteristics/bandgaps of the prepared CsPbBr₃ NCs on the synthesis temperature and the total flow rate through the microfluidic system. Using the PL characteristics of the prepared CsPbBr₃ NCs, we determine the activation energy for the rate process controlling the growth of the prepared CsPbBr₃ NCs and observe that a higher total flow rate can reduce the dispersity of the CsPbBr₃ NCs.

Experimental Details

Chemicals

The materials used were CsBr (99.9%, Beantown Chemical), PbBr₂ (>98%, Strem Chemicals Inc.), N,N-dimethylformamide (DMF) (VWR), oleylamine (OAm) (>50%, TCI America), oleic acid (OA) (Ward's Science), toluene (VWR). The as-received materials were used without any purification.

Preparation of precursor solution for CsPbBr₃ NCs

A solution of 10 mL DMF, 1 mL OA and 0.5 mL OAm was placed in a glass vial with equimolar (0.4 mol) CsBr and PbBr₂ powders to form a mixture. A precursor solution was prepared after heating the mixture at 303 K overnight under vigorous stirring.

Microfluidic platform

Figure 1 shows schematically the set-up of the microfluidics platform used in this work. Two syringe pumps (Harvard Apparatus) were used to support two syringes. The two syringes were filled with the precursor solution and antisolvent (toluene), respectively. A mini-vial (1 cm³ in volume), which was connected to the two syringes through two PTFE capillaries (0.8 mm in inner diameter and 80 cm in length) and fixed to a

temperature-controllable hot plate, was used as the miniaturized reactor for the formation and growth of CsPbBr₃ NCs. A third capillary of 0.8 mm in inner diameter and 60 cm in length was used to transport the liquid (the precursor solution and antisolvent) from the miniaturized reactor to a large glass vial. Continuous growth of CsPbBr₃ NCs occurred also in the third capillary tube; the large glass vial placed in a cooling system (ice-water bath) was used to collect the suspension consisting of CsPbBr₃ NCs. The flow rates of the precursor solution and antisolvent in the capillary tubes were controlled by the syringe pumps.

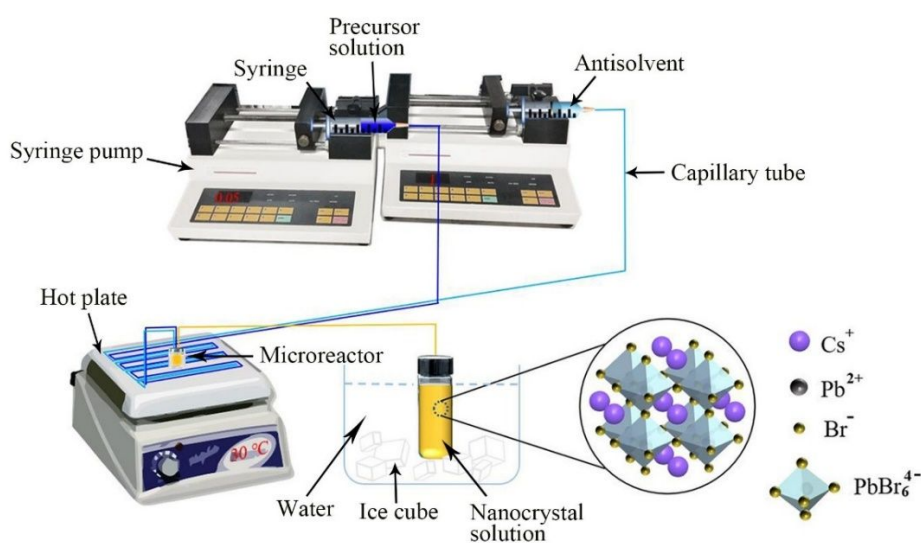


Figure 1. Schematic of the microfluidic platform used for the preparation of CsPbBr₃ NCs of cubic structure as circled by the solid black line.

Synthesis of CsPbBr₃ NCs in the microfluidic platform

The synthesis of CsPbBr₃ NCs was based on an antisolvent method,⁴⁸ which is also referred to as a reprecipitation method.⁵² Specially, the perovskite precursor solution and toluene (antisolvent) were flowed into the miniaturized reactor with a flow rate ratio of 1 to 20 (perovskite precursor solution to toluene) to maintain the same volume ratio of 1:20 for different flow rates. The two solutions were mixed in the miniaturized reactor (the mini-vial), leading immediately to the formation of CsPbBr₃ NCs. It took less than three seconds to form CsPbBr₃ NCs.⁴⁸ The mixed solution with the formed CsPbBr₃ NCs was then flowed from the miniaturized reactor into the large glass vial, which was placed in an ice-water bath, for the collection of the formed CsPbBr₃ NCs. The ice-water bath was used to limit the formed CsPbBr₃ NCs from further growth¹² and rapid fouling due to the increase in the NC sizes.⁵³

Note that the growth of NCs is related to the frequency of monomers attaching to the clusters/NCs, i.e., the higher the frequency, the larger is the NCs.⁵⁴ The attachment frequency increases with increasing temperature.⁵⁴ Lowering the temperature of a NC solution can retard the growth of NCs in the solution to some extent.

It should be noted that precipitation is a universal phenomenon during the preparation of nanocrystals, which is due to increase in the sizes of NCs through the coalescence (growth) of NCs. It generally uses a cooling system to lower the synthesis temperature and limit the growth (coalescence) of NCs. The rapid fouling and precipitation of NCs in a microfluidic system is dependent on the flow rate, growth temperature and relative size of NCs to the diameter of the flow channels. Increasing the flow speed, reducing the concentration of NCs and lowering the growth temperature can hinder the rapid fouling and precipitation of NCs in a microfluidic system. Note that fouling and precipitation of NCs in two-phase or multi-phase flow system can also occur, depending on the sizes of NCs possibly grown in the system (droplets).

Four different flow rates of 0.05, 0.10, 0.20 and 0.30 mL/min were used for the precursor solution. The synthesis of the CsPbBr₃ NCs in the microfluidic platform was conducted at four different temperatures of 303, 323, 343 and 363 K. Both the syringe pumps with the precursor solution and antisolvent were pre-heated to a pre-determined reaction temperature prior to being flowed into the miniaturized reactor, and the miniaturized reactor and the capillary connecting the miniaturized reactor to the NC-collection vial were placed on a hot plate and maintained at the pre-determined reaction temperature. Most the capillaries connecting the pumps to the miniaturized reactor were placed on the hot plate and maintained at pre-determined reaction temperature. This limited the heat loss and was able to maintain the reaction temperature to a reasonable degree. A piece of asbestos (50×50×1.7 cm³) was used to cover the system (pump, capillaries and hot plate) to maintain a stable and uniform temperature. It should be noted that some NCs might not flow out the miniaturized reactor immediately at a low flow rate. However, this did not likely play any important role in the growth of the NCs since the analysis was based on average size of NCs. A batch-to-batch preparation of CsPbBr₃ NCs was carried out for 5 times, and the average results from the five

tests were used in the kinetic analysis. To evaluate the feasibility of the proposed microfluidic platform for long-time continuous manufacturing of CsPbBr₃ NCs, the batch-to-batch preparation of CsPbBr₃ NCs on the same microfluidic system under the same growth conditions was performed continuously (for five times) without cleaning the system. No blockage of the microfluidic system occurred.

Characterization

PL characterization of the liquid solution with the formed CsPbBr₃ NCs in the large glass vial was conducted immediately on a miniature spectrometer (Ocean optics) after the completion of the flow. The XRD (X-ray diffraction) characterization of the crystal structure of the formed CsPbBr₃ NCs was performed on a diffractometer (Siemens D-500) with a radiation of CuK_α ($\lambda=1.54060$ Å). The sample preparation for the XRD characterization of the formed CsPbBr₃ NCs involved the centrifugation of the liquid solution with the formed CsPbBr₃ NCs at 8000 rpm for 5 min and the evaporation of the solvent residuals in the collected sediments from the centrifugation in air. Note that the coalescence of the formed CsPbBr₃ NCs likely occurred during the sample preparation for the XRD characterization. The geometrical characteristics of the formed CsPbBr₃ NCs were examined on a transmission electron microscope (TEM) (Thermo-scientific Talos F200X) at an accelerating voltage of 200 kV. The sample for the TEM characterization was obtained directly from the liquid solution with the formed CsPbBr₃ NCs in the large glass vial immediately after the finish of the synthesis in contrast to the sample preparation for the XRD characterization, which likely limited the coalescence effect on the sizes of the formed CsPbBr₃ NCs.

Results

The formation of CsPbBr₃ NCs is dependent on the solubility of CsPbBr₃ in a solvent. CsBr, PbBr₂ and CsPbBr₃ crystals have large solubilities in the polar solvent of DMF, resulting in the presence of Cs⁺, Pb²⁺ and Br⁻ in the precursor solution. When the precursor solution is mixed with nonpolar solvent of toluene, the nucleation of CsPbBr₃ clusters occurs, leading to the formation of CsPbBr₃ NCs. OA and OAm interact with the CsPbBr₃ NCs and form a protection layer (ligands) on the CsPbBr₃ NCs (NC-ligand structure) to hinder the growth of the CsPbBr₃ NCs and cause the dispersion of the NC-ligand structures in toluene.

Define total flow rate as the summation of the flow rate of the precursor solution and the flow rate of toluene. We have total flow rates of 1.05, 2.1, 4.2 and 6.3 mL/min, corresponding to 0.05, 0.10, 0.20 and 0.30 the mL/min of the flow rates of the precursor solution, respectively.

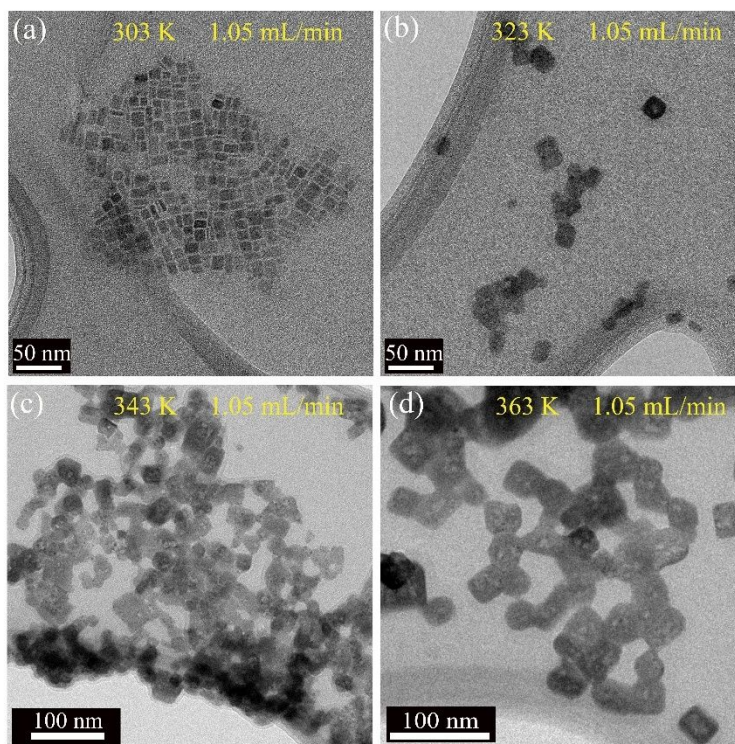


Figure 2. TEM images of the CsPbBr₃ NCs formed at four different temperatures for the total flow rate of 1.05 mL/min: (a) 303 K, (b) 323 K, (c) 343 K, and (d) 363 K. (Total flow rate = flow rate of precursor solution + flow rate of toluene)

Figure 2 presents TEM images of the CsPbBr₃ NCs formed at four different temperatures for the total flow rate of 1.05 mL/min. It is evident that the size of NCs increases with increasing temperature. Using the TEM images, the size distribution of the formed CsPbBr₃ NCs is determined and presented in Fig. S1 in Supplementary Information. From the size distribution of the formed CsPbBr₃ NCs, we obtain average sizes of $\sim 13 \pm 2$, $\sim 20 \pm 3$, $\sim 27 \pm 2$ and $\sim 34 \pm 4$ nm for the CsPbBr₃ NCs formed at four different temperatures of 303, 323, 343 and 363 K, respectively, for the total flow rate of 1.05 mL/min.

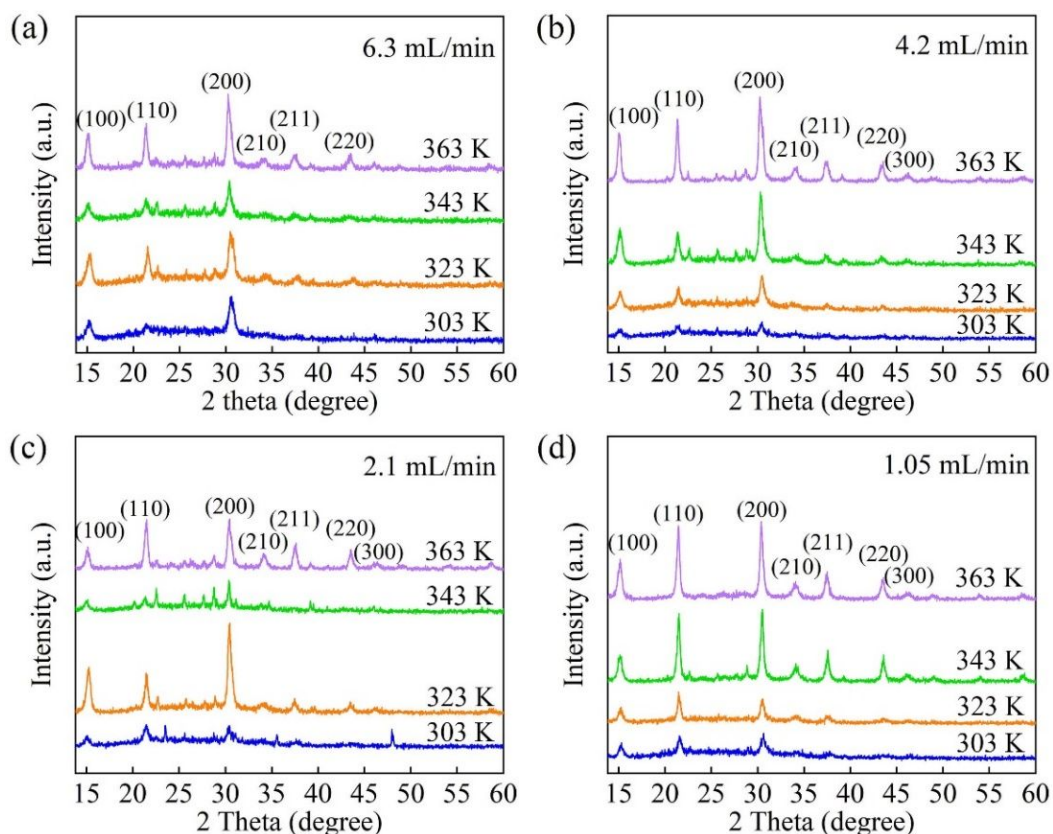


Figure 3. XRD patterns of the CsPbBr₃ NCs prepared at four different temperatures of 303, 323, 343 and 363 K for different total flow rates of (a) 6.3 mL/min, (b) 4.2 mL/min, (c) 2.1 mL/min, and (d) 1.05 mL/min. The XRD patterns are in consistency with PDF card#54-0752.

Figure 3 depicts XRD patterns of the formed CsPbBr₃ NCs at four different temperatures for different total flow rates. All the XRD patterns are generally in good concordance with PDF card#54-0752, confirming cubic structure of the formed CsPbBr₃ NCs. Such a result suggests that the crystal structure of the formed CsPbBr₃ NCs is independent of the temperature and flow rate used in this work. The two theta angles of $\sim 15^\circ$, $\sim 22^\circ$, $\sim 31^\circ$, $\sim 34^\circ$, $\sim 38^\circ$, $\sim 44^\circ$ and $\sim 47^\circ$ for the XRD peaks presented in Fig. 3 correspond to (100), (110), (200), (210), (211), (220) and (300) planes, respectively. Note that the XRD-peak intensities increase with the increase of temperature and the full width at half maximum (FWHM) of the peak is smaller at a higher temperature. The decrease of the FWHM with increasing temperature can be likely attributed to the increase of the NC size.⁵⁵ A large lattice strain due to the defects introduced at a high temperature can also lead to a large FWHM of a XRD peak.

Using the Scherrer equation, $D = K\lambda/\beta\cos\theta$ (D , K , λ , β and θ are average crystallite size,

shape factor, wavelength of X-ray, half width of XRD peak and diffraction angle, respectively), we calculate average sizes of the CsPbBr₃ NCs formed at different temperatures for different flow rates. The average sizes of the CsPbBr₃ NCs are listed in Table S1 in Supplementary Information. It is evident that the average crystal size of the formed CsPbBr₃ NCs increases with the decrease of the flow rate at the same synthesis temperature and increases with the increase of the synthesis temperature for the same flow rate, as expected. Note that there are some differences between the average crystal sizes of the formed CsPbBr₃ NCs determined from the TEM images and the corresponding ones determined from the XRD analysis for the total flow rate of 1.05 mL/min. Such differences can be likely attributed to the following reasons. TEM images are two-dimensional and the crystal size in the depth direction is unknown. The average crystal size is calculated from two-dimensional information. TEM images only provide the information of local area with small amounts of samples. XRD patterns contain three-dimensional information from large amounts of samples, and the average crystal size is calculated from much large numbers of crystals.

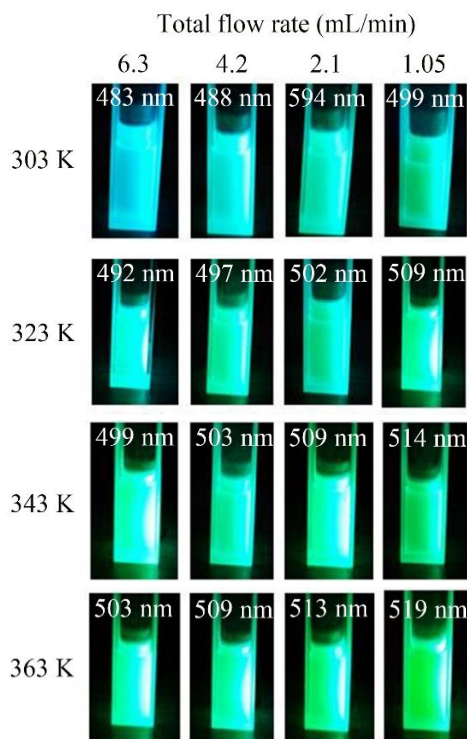


Figure 4. Optical images of the suspensions of the prepared CsPbBr₃ NCs in cuvettes prepared with different flow rates at different temperatures under UV light of 365 nm in

wavelength.

Figure 4 shows optical images of the suspensions of the CsPbBr₃ NCs under UV light of 365 nm in wavelength, which were prepared with different total flow rates at different temperatures. The CsPbBr₃ NCs in the solution prepared at 303 K with the total flow rate of 6.3 mL/min emitted blue-green light (483 nm wavelength). Increasing the synthesis temperature and/or decreasing the flow rate cause the increase in the emission wavelength of the CsPbBr₃ NCs in the solution. For example, the CsPbBr₃ NCs in the solution prepared at 363 K with the total flow rate of 1.05 mL/min emitted yellow-green light (519 nm in wavelength). Such a change in the color of the emission light can be attributed to the size dependence of the CsPbBr₃ NCs on the synthesis conditions, including temperature and flow rate.

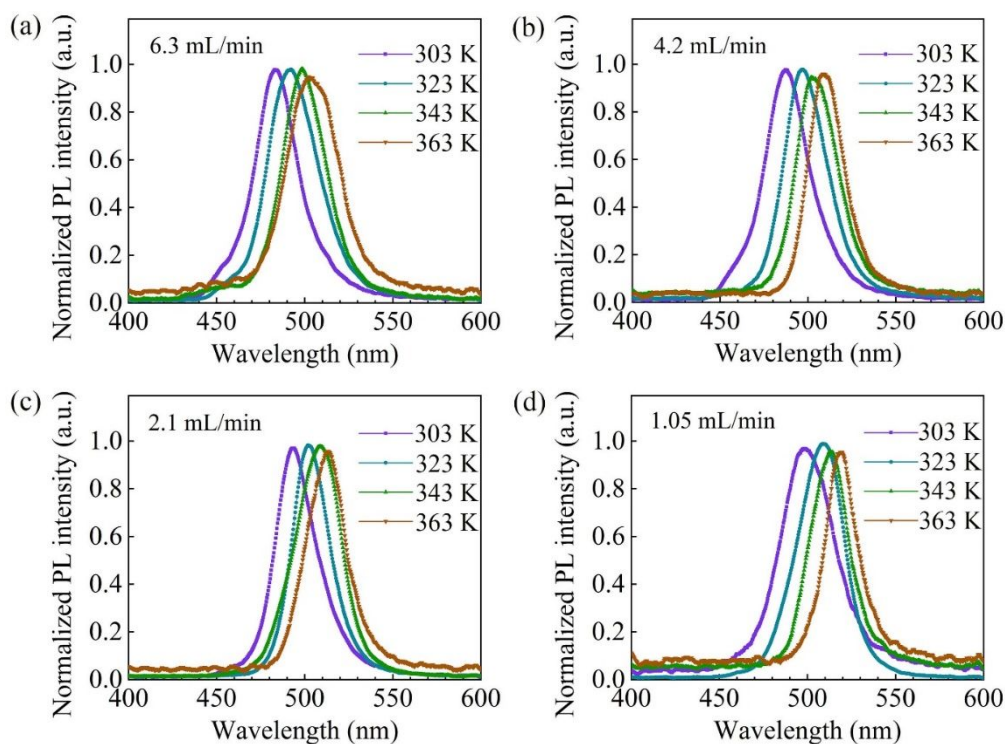


Figure 5. PL spectra of the CsPbBr₃ NCs prepared at four different temperatures with different total flow rates under UV light of 365 nm in wavelength: (a) 6.3 mL/min, (b) 4.2 mL/min, (c) 2.1 mL/min, and (d) 1.05 mL/min.

The normalized PL spectra of the prepared CsPbBr₃ NCs are presented in Fig. 5 and Fig. S2 in Supplementary Information. According to Fig. 5a-d, increasing the synthesis temperature caused red shift of the PL peak wavelength for the prepared CsPbBr₃ NCs under

the same total flow rate. From Fig. S2, we note blue shift of the PL peak wavelength for the prepared CsPbBr₃ NCs with the increase of the total flow rate at the same synthesis temperature. For example, the PL peak wavelength increases from 483 nm to 503 nm with the increase of the synthesis temperature from 303 to 363 K for the total flow rate of 6.3 mL/min and from 483 nm to 499 nm with the decrease of the total flow rate from 6.3 mL/min to 1.05 mL/min at the synthesis temperature of 303 K. Table 1 summaries the PL peak wavelength of the prepared CsPbBr₃ NCs.

Using the PL peak wavelength and the relation between bandgap and the PL peak wavelength, $E = hc/\lambda q$ in the unit of eV (h , c , λ and q are the Planck constant, light speed in vacuum, emission wavelength of photon and electron charge, respectively), the bandgaps of the prepared CsPbBr₃ NCs are calculated and listed in Table 1. It is evident that the bandgap decreases with the increase of the synthesis temperature for the same flow rate and with the decrease of the total flow rate at the same synthesis temperature. The repeated batch-to-batch preparation for the CsPbBr₃ NCs for 5 times reveals insignificant standard deviations of the PL-peak wavelength for the NCs prepared under the same conditions, suggesting reproducible nanocrystal synthesis.

Table 1. Wavelengths and bandgaps of the CsPbBr₃ NCs prepared by different flow rates and temperatures

Temperature	Wavelength (nm)/Bandgap (eV)			
	6.3 mL/min	4.2 mL/min	2.1 mL/min	1.05 mL/min
303 K	483.3±0.3/2.566±0.003	488.3±0.7/2.539±0.007	493.7±0.5/2.512±0.005	499.0±0.6/2.485±0.006
323 K	491.9±0.5/2.521±0.005	497.2±1.0/2.494±0.010	502.4±0.4/2.468±0.004	509.3±0.4/2.435±0.004
343 K	499.3±1.0/2.483±0.010	502.5±0.3/2.468±0.003	509.3±0.5/2.435±0.005	514.0±0.2/2.412±0.002
363 K	503.3±0.4/2.464±0.004	509.2±0.8/2.435±0.008	512.9±0.6/2.418±0.006	519.0±0.9/2.389±0.009

Discussion

It is known that the PL peak wavelength of semiconductor NCs is dependent on average size of the semiconductor NC, which can be referred to the quantum confinement effect. According to the quantum confinement effect, the bandgap of a semiconductor NC, E , at temperature, T (absolute temperature), as a function of the characteristic size of the semiconductor nanocrystal, a , can be expressed as⁵⁶⁻⁵⁸

$$E(T) = E_0(T) + \frac{h^2}{2(m_e^* + m_h^*)} \frac{1}{a^2} \equiv E_0(T) + \frac{\alpha}{a^2} \quad (2)$$

where $E_0(T)$ is the bandgap of the bulk phase of the corresponding semiconductor at temperature, T , m_e^* and m_h^* are the reduced masses of electron and hole, respectively. Note that Eq. (2) is based on that the contribution of the Coulomb interaction to the bandgap of the semiconductor NC is negligible.

The variation of the PL peak wavelength of the prepared CsPbBr₃ NCs with the synthesis temperature and the total flow rate suggests the size dependence of the prepared CsPbBr₃ NCs on the synthesis temperature and the flow rate, i.e., the growth of the CsPbBr₃ NCs in the microfluidic platform is dependent on the synthesis temperature and the growth time (flow rate). For diffusion-dominant growth process, the time dependence of the characteristic size of a semiconductor nanocrystal can be expressed as^{59, 60}

$$a^2 = Dt \quad (3)$$

with D as the diffusion coefficient of monomers in the liquid solution, and t as the growth time. The temperature dependence of the diffusion coefficient follows the Arrhenius relation as

$$D = D_0 e^{-Q/RT} \quad (4)$$

where D_0 is a pre-factor, Q is the activation energy for the diffusion of the monomers in the liquid solution, and R is the gas constant.

Using the flow rates and the materials properties (densities and viscosities) of DMF and toluene, we estimated the viscosity of the liquid suspensions and calculated the Reynolds numbers for the corresponding flow rates (Table S2 in Supplementary Information). The largest Reynolds number corresponding to the total flow rate of 6.3 mL/min is 266, suggesting that the flow in the microfluidics is laminar for the flow rates used in this work. Note that the Reynolds number for the outset of the transition from laminar flow to turbulent flow is ~ 2300 for a pipe flow. Corresponding to the total flow rate of 6.3 mL/min, the average flow speed is 20.9 mm/s. Yang⁶¹ noted a $\sim 15\%$ increase in the change of the Gibbs free energy for the average flow speed being increased from 2 mm/s to 20 mm/s in the study of homogeneous nucleation in a Poiseuille flow. This change suggests the effect of convection on the growth of NCs in the microfluidic system is limited and the growth is not in a mass-transfer-limited regime. Thus, it is reasonable to assume that the contribution of convection from the flow to the growth of CsPbBr₃ NCs in the microfluidic system is negligible⁶¹ and the growth time of the CsPbBr₃ NCs in the microfluidic platform is inversely proportional to the total flow rate, F , as

$$t \propto F^{-1} \quad (5)$$

Note that Eq. (1) is based on that the geometrical dimensions and structure of the microfluidic platform remain unchanged for the growth conditions used in this work.

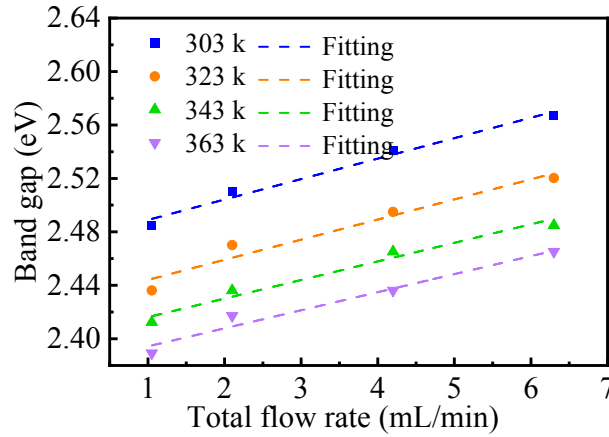


Figure 6. Variation of the bandgap of the prepared CsPbBr₃ NCs with total flow rate at different synthesis temperatures.

Substituting Eqs. (3)-(5) in Eq. (2) yields

$$E(T) = E_0(T) + \beta e^{Q/RT} F \quad (6)$$

where β is a constant proportional to α and D_0^{-1} . Figure 6 shows the variation of the bandgap of the prepared CsPbBr₃ NCs with the total flow rate at different synthesis temperatures. It is evident that the bandgap of the CsPbBr₃ NCs prepared at the same synthesis temperature is a linear function of the flow rate, supporting Eq. (6). Using linear regression to fit the experimental results shown in Fig. 6, we obtain $E_0(T)$ and $\beta e^{Q/RT}$.

According to the relation given by Varshni⁶², the temperature dependence of the bandgap of a bulk semiconductor can be expressed as

$$E_0(T) = E_0 - \frac{bT^2}{T + c} \quad (7)$$

with E_0 as the bandgap of the semiconductor at 0 K, b and c are two constants. It is known that bulk CsPbBr₃ can be presented in orthorhombic, tetragonal and cubic structure in the temperature range of 0 to 353 K, 273 to 403 K and 403 K above, respectively⁶³. That is to say, bulk CsPbBr₃ can be seldomly presented in cubic structure at 0 K. To estimate the numerical value of E_0 for cubic CsPbBr₃ at 0 K, we linearly extrapolate the numerical results given by Mannino et al.⁶⁴ and obtain $E_0 \approx 2.29$ eV.

Figure 7 depicts the temperature dependence of $E_0(T) - E_0$. The bandgap of the bulk CsPbBr₃ of cubic structure exhibits a decreasing trend with the increase of temperature. Eq. (7) is used to fit the data in Fig. 7. For comparison, the fitting curve is also included in Fig. 7.

It is evident that Eq. (7) describes well the temperature dependence of $E_0(T)$. From the curve fitting, we obtain $b = -6.99 \times 10^{-5}$ eV/K and $c = -267.84$ K for the temperature in a range of 303 to 363 K.

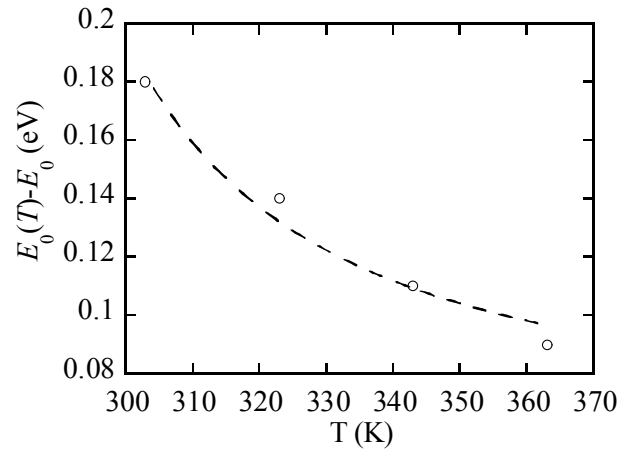


Figure 7. Temperature dependence of $E_0(T) - E_0$ for the prepared CsPbBr₃ NCs.

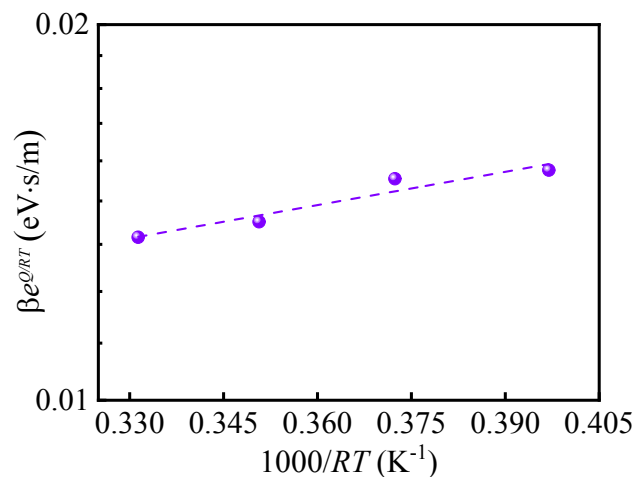


Figure 8. Temperature dependence of $\beta e^{Q/RT}$ for the prepared CsPbBr₃ NCs.

To determine the activation energy for the rate process controlling the growth of the CsPbBr₃ NCs in the microfluidic platform, we plot the temperature dependence of $\beta e^{Q/RT}$ in Fig. 8. It is evident that the logarithm of $\beta e^{Q/RT}$ is a linear function of T^{-1} . Using the linear relation between logarithm of $\beta e^{Q/RT}$ and T^{-1} to fit the data in Fig. 8, we obtain an activation energy of 2.05 kJ/mol for the diffusion of monomers in the liquid solution under the flow environment, which controls the growth of the CsPbBr₃ NCs in the microfluidic platform for the conditions used in this work.

According to Eq. (2), there is a linear relationship between the bandgap and the characteristic size of a semiconductor NC, which is the foundation for the above analysis. Figure 9 depicts the variation of the bandgap with the reciprocal of the square of the average

size of the CsPbBr₃ NCs formed in the microfluidic platform for the total flow rate of 1.05 mL/min. Both the average sizes of the CsPbBr₃ NCs determined from the TEM images and XRD analyses are included in Fig. 9. In general, the bandgap is an approximately linearly increasing function of the reciprocal of the square of the average size of the CsPbBr₃ NCs in good accordance with Eq. (2) for both groups of data. Such a result supports the method used in this work to analyze the growth behavior of the CsPbBr₃ NCs synthesized in the microfluidic platform. It needs to be pointed out that there are some differences between the average sizes of the CsPbBr₃ NCs determined from the XRD and the corresponding ones determined from the TEM images. As discussed above, TEM images are two-dimensional without information of the crystal size in the depth direction and the average crystal size is calculated from two-dimensional information. TEM images only provide the information of local area with small amounts of samples. XRD patterns contain three-dimensional information from large amounts of samples, and the average crystal size is calculated from much large numbers of crystals. Also, the centrifugation and drying for the preparation of the XRD samples might cause the coalescence of the CsPbBr₃ NCs, leading to the increase of the average crystal size determined from the XRD analyses.

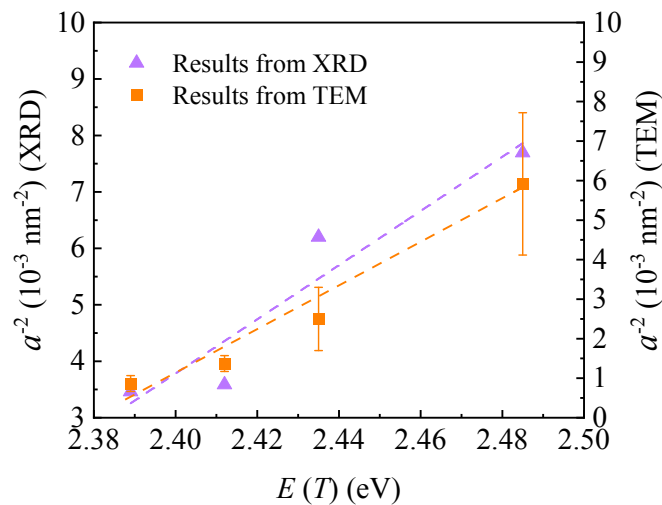


Figure 9. Size dependence of the bandgap.

In the following analysis, the average crystal sizes of the CsPbBr₃ NCs determined from the XRD analyses are used in the corresponding calculations. Using Eq. (2), we have the bandgap difference at half maximum of the PL peak of the CsPbBr₃ NCs, ΔE_{FWHM} , as

$$\Delta E_{\text{FWHM}} = \frac{\alpha}{(a - \Delta a / 2)^2} - \frac{\alpha}{(a + \Delta a / 2)^2} \approx \frac{2\alpha\Delta a}{a^3} \quad (8)$$

for $a \gg \Delta a$. Here, Δa is the size difference between the CsPbBr₃ NCs at $E - \Delta E_{\text{FWHM}}/2$ and those at $E + \Delta E_{\text{FWHM}}/2$. It is evident that ΔE_{FWHM} is proportional to Δa , as revealed in Eq. (8).

Figure 10 presents the variation of $\Delta E_{\text{FWHM}} \cdot a^3$ with the total flow rate. It is evident that the numerical values of $\Delta E_{\text{FWHM}} \cdot a^3$ for the CsPbBr₃ NCs prepared at the same temperature decrease with the increase of the total flow rates for all the four temperatures of 303, 323, 343 and 363 K. Such a trend reveals that the total flow rate plays a role in the dispersity of the CsPbBr₃ NCs grown in the microfluidic system. The higher the total flow rate, the smaller is the dispersity of the CsPbBr₃ NCs. From Fig. 10, we note that increasing the growth temperature generally caused the increase of the numerical values of $\Delta E_{\text{FWHM}} \cdot a^3$ for the same total flow, indicating the increase of the dispersity of the CsPbBr₃ NCs grown at high temperatures. Note that the numerical value of $\Delta E_{\text{FWHM}} \cdot a^3$ for the CsPbBr₃ NCs grown at 363 K is larger than that grown at 343 K for the total flow rate of 1.05 mL/min. The reason for such an opposite trend is unclear, and it might be due to experimental errors.

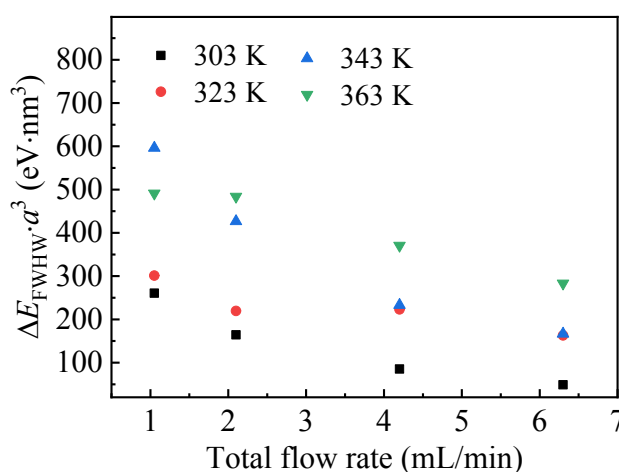


Figure 10. Variation of $\Delta E_{\text{FWHM}} \cdot a^3$ with the total flow rate for the CsPbBr₃ NCs prepared at different temperatures. Here, the average crystal sizes of the CsPbBr₃ NCs determined from the XRD analyses are used in the calculation.

There are two process variables controlling the growth time: one is the total flow rate and the other is the capillary length between the miniaturized reactor and the large glass vial. Increasing the capillary length and decreasing the total flow rate can increase the growth time of CsPbBr₃ NCs. To evaluate the effects of the capillary length between the miniaturized reactor and the large glass vial on the PL characteristics and the size evolution of CsPbBr₃ NCs, we prepared CsPbBr₃ NCs from the same microfluidic system with different capillary lengths (20, 40, 60 and 80 cm) between the miniaturized reactor and the large glass vial for a total flow rate of 1.05 mL/min at 303 K. Figure S3-4 present the PL spectra and XRD patterns of the CsPbBr₃ NCs prepared for four different capillary lengths. The corresponding PL peak wavelengths and average crystal sizes of the prepared CsPbBr₃ NCs are summarized

in Table 2.

Using the experimental data in Table 2, the variations of the PL peak wavelength and the square of average crystal size with the capillary length is depicted in Fig. 11. It is evident that both the PL peak wavelength and the square of average crystal size are linearly increasing functions of the capillary length, suggesting the linear correlation between the PL peak wavelength (reciprocal of the bandgap) and the square of average crystal size. This result supports Eq. (2) for the CsPbBr₃ NCs grown under the same growth conditions with different capillary lengths. For a constant total flow rate, the time for the CsPbBr₃ NCs grown in the microfluidic system is a linearly increasing function of the capillary length. Thus, there exists a linear relation between the growth time and the square of average crystal size, which again suggests the diffusion of monomers as the dominant mechanism for the growth of CsPbBr₃ NCs in the microfluidic system.

Table 2. PL peak wavelengths and average crystal sizes of the CsPbBr₃ NCs prepared for a total flow rate of 1.05 mL/min at 303 K with four different capillary lengths

Temperature	Flow rate	Wavelength (nm)/Average size (nm)			
		20 cm	40 cm	60 cm	80 cm
303 K	1.05 mL/min	493.2±1.0/10.1	497.1±0.4/10.9	499.5±0.5/11.5	502.3±0.9/12.0

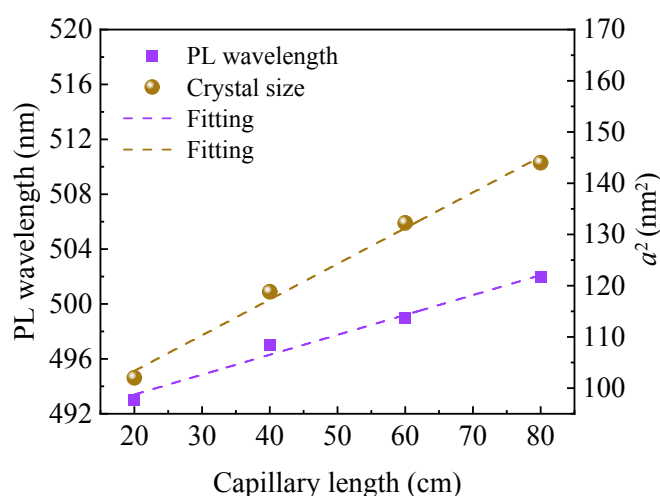


Figure 11. Variations of PL peak wavelength and square of average crystal size of the CsPbBr₃ NCs prepared with different capillary lengths. (Total flow rate: 1.05 mL/min, temperature: 303 K)

Conclusion

Microfluidics has provided a platform to continuously fabricate nanoparticles and semiconductor nanocrystals. We have used a PTFE-based microfluidic system and the antisolvent principle to continuously synthesize CsPbBr₃ NCs in a temperature range of 303

to 363 K for the total flow rates of 1.05, 2.1, 4.2 and 6.3 mL/min. Both the TEM and XRD analyses have confirmed the production of CsPbBr₃ NCs of cubic structure and found the dependence of the average size of the prepared CsPbBr₃ NCs on the synthesis conditions, including the flow rate, the capillary length and the synthesis temperature. There exist differences of the average sizes of the prepared CsPbBr₃ NCs with the total flow rate of 1.05 mL/min between the results from the TEM analysis and those from the XRD analysis. Such differences can be attributed to the difference in the sampling sizes and the possible coalescence of NCs during the centrifugation and drying – TEM images were obtained from limited amounts of NCs and captured two-dimensional features of NCs, and XRD analyses used significantly large amounts of NCs which might experience coalescence during the centrifugation and drying.

We have developed a relationship between the bandgap (the PL peak wavelength) and the total flow rate (the growth time) for the growth of semiconductor nanocrystals in a microfluidic system from the size-dependence of the bandgap of semiconductor nanocrystals (the quantum confinement effect) under the condition that the contribution of the Coulomb interaction to the quantum confinement is negligible. Using this relationship and the PL characteristics of the prepared CsPbBr₃ NCs, we have analyzed the growth behavior of the CsPbBr₃ NCs prepared in the microfluidic system and found the proportionality between the reciprocal of the square of the average size of the CsPbBr₃ NCs and the total flow rate and between the square of the average size of the CsPbBr₃ NCs and the capillary length between the miniaturized reactor and the NC-collection outlet. Such results suggest that the diffusion of monomers in the liquid solution is the dominant rate process controlling the growth of the CsPbBr₃ NCs in the microfluidic system. The activation energy for the rate process is 2.05 kJ/mol, and the temperature dependence of the bandgap of the bulk CsPbBr₃ crystals of cubic structure follows the empirical relation developed by Varshni⁶².

We have derived a relation between the difference of the bandgaps at half maximum of the PL peak and the corresponding size difference from the relation between the bandgap and the average size of semiconductor NCs, Using this relation, we have analyzed the effects of the synthesis temperature and the total flow rate on the size distribution of the prepared

CsPbBr₃ NCs. The analysis reveals that increasing the synthesis temperature widens the size distribution of the CsPbBr₃ NCs prepared in the microfluidic platform.

It is worth mentioning that the relationship between the bandgap (the PL peak wavelength) and the total flow rate (the growth time) for the growth of semiconductor nanocrystals provides the basis to analyze the growth behavior of semiconductor nanocrystals under dynamic conditions from in-situ measurement of the PL characteristics of the semiconductor nanocrystals. Such an approach avoids the use of TEM and XRD techniques, which likely involve the coalescence of semiconductor nanocrystals during the sample processing and/or under e-beam and X-ray and limited amounts of NCs used in TEM imaging, and can be extended to in-situ study the growth behavior of other semiconductor nanocrystals under a variety of synthesizing conditions.

Conflicts of interest

The authors declare no conflict of interest.

Acknowledgements

FY is grateful for the support by the NSF through the grant CMMI-1854554, monitored by Drs. Khershed Cooper and Thomas Francis Kuech, and CBET- 2018411 monitored by Dr. Nora F Savage.

References

1. E. K. Sackmann, A. L. Fulton and D. J. Beebe, *Nature*, 2014, **507**, 181-189.
2. X. Mao and T. J. Huang, *Lab on a Chip*, 2012, **12**, 1412-1416.
3. D. R. Walt, *Science*, 2005, **308**, 217-219.
4. Y. Xia, J. Si and Z. Li, *Biosensors and Bioelectronics*, 2016, **77**, 774-789.
5. M. L. Adams, M. Enzelberger, S. Quake and A. Scherer, *Sensors and Actuators A: Physical*, 2003, **104**, 25-31.
6. Y. Zilberman, S. K. Ameri and S. R. Sonkusale, *Sensors and Actuators B: Chemical*, 2014, **194**, 404-409.
7. C. M. B. Ho, S. H. Ng, K. H. H. Li and Y.-J. Yoon, *Lab on a Chip*, 2015, **15**, 3627-3637.
8. A. K. Au, W. Huynh, L. F. Horowitz and A. Folch, *Angewandte Chemie International Edition*, 2016, **55**, 3862-3881.

9. A. V. Nielsen, M. J. Beauchamp, G. P. Nordin and A. T. Woolley, *Annual Review of Analytical Chemistry*, 2020, **13**, 45-65.
10. A. Jahn, J. E. Reiner, W. N. Vreeland, D. L. DeVoe, L. E. Locascio and M. Gaitan, *Journal of Nanoparticle Research*, 2008, **10**, 925-934.
11. D. Desai, Y. A. Guerrero, V. Balachandran, A. Morton, L. Lyon, B. Larkin and D. E. Solomon, *Nanomedicine: Nanotechnology, Biology and Medicine*, 2021, 102402.
12. L. Protesescu, S. Yakunin, M. I. Bodnarchuk, F. Krieg, R. Caputo, C. H. Hendon, R. X. Yang, A. Walsh and M. V. Kovalenko, *Nano Letters*, 2015, **15**, 3692-3696.
13. F. P. García de Arquer, D. V. Talapin, V. I. Klimov, Y. Arakawa, M. Bayer and E. H. Sargent, *Science*, 2021, **373**, eaaz8541.
14. Q. A. Akkerman, G. Rainò, M. V. Kovalenko and L. Manna, *Nature Materials*, 2018, **17**, 394-405.
15. W. Chi and S. Banerjee, *Angewandte Chemie*.
16. Y. Bai, M. Hao, S. Ding, P. Chen and L. Wang, *Advanced Materials*, 2021, 2105958.
17. Y. Wei, Z. Cheng and J. Lin, *Chemical Society Reviews*, 2019, **48**, 310-350.
18. J. Shamsi, A. S. Urban, M. Imran, L. De Trizio and L. Manna, *Chemical Reviews*, 2019, **119**, 3296-3348.
19. Y. He, L. Matei, H. J. Jung, K. M. McCall, M. Chen, C. C. Stoumpos, Z. Liu, J. A. Peters, D. Y. Chung and B. W. Wessels, *Nature Communications*, 2018, **9**, 1-8.
20. D. N. Dirin, I. Cherniukh, S. Yakunin, Y. Shynkarenko and M. V. Kovalenko, *Chemistry of Materials*, 2016, **28**, 8470-8474.
21. I. G. Koryakina, M. Naumochkin, D. I. Markina, S. A. Khubezhov, A. P. Pushkarev, A. A. Evstrapov, S. V. Makarov and M. V. Zyuzin, *Chemistry of Materials*, 2021, **33**, 2777-2784.
22. Z. Bao, J.-W. Luo, Y.-S. Wang, T.-C. Hu, S.-Y. Tsai, Y.-T. Tsai, H.-C. Wang, F.-H. Chen, Y.-C. Lee and T.-L. Tsai, *Chemical Engineering Journal*, 2021, 130849.
23. C. Zhang, W. Luan, Y. Huang and F. Yang, *Nanotechnology*, 2019, **30**, 145602.
24. S. Marre and K. F. Jensen, *Chemical Society Reviews*, 2010, **39**, 1183-1202.

25. S. Kubendhiran, Z. Bao, K. Dave and R.-S. Liu, *ACS Applied Nano Materials*, 2019, **2**, 1773-1790.
26. R. W. Epps, K. C. Felton, C. W. Coley and M. Abolhasani, *Lab on a Chip*, 2017, **17**, 4040-4047.
27. I. Lignos, S. Stavrakis, G. Nedelcu, L. Protesescu, A. J. deMello and M. V. Kovalenko, *Nano Letters*, 2016, **16**, 1869-1877.
28. K. Ma, X.-Y. Du, Y.-W. Zhang and S. Chen, *Journal of Materials Chemistry C*, 2017, **5**, 9398-9404.
29. K. Abdel-Latif, R. W. Epps, F. Bateni, S. Han, K. G. Reyes and M. Abolhasani, *Advanced Intelligent Systems*, 2021, **3**, 2000245.
30. S. Li, R. W. Baker, I. Lignos, Z. Yang, S. Stavrakis, P. D. Howes and A. J. deMello, *Molecular Systems Design & Engineering*, 2020, **5**, 1118-1130.
31. Y. Geng, J. Guo, S. D. Ling, X. Wu, H. Liu, Z. Chen, S. Chen and J. Xu, *Science China Materials*, 2022, 1-9.
32. R. Guo, Y. Liu, Y. Fang, Z. Liu, L. Dong, L. Wang, W. Li and J. Hou, *CrystEngComm*, 2022, **24**, 3852-3858.
33. Z. Bao, H.-C. Wang, Z.-F. Jiang, R.-J. Chung and R.-S. Liu, *Inorganic Chemistry*, 2018, **57**, 13071-13074.
34. Y. Yu, J. Guo, F. Bian, D. Zhang and Y. Zhao, *Science China Materials*, 2021, **64**, 2858-2867.
35. R. Cheng, Z. B. Liang, L. Zhu, H. Li, Y. Zhang, C. F. Wang and S. Chen, *Angewandte Chemie*, 2022, e202204371.
36. F. Bian, L. Sun, Y. Wang, D. Zhang, Z. Li and Y. Zhao, *Science China Chemistry*, 2021, **64**, 1540-1546.
37. K. Abdel-Latif, R. W. Epps, C. B. Kerr, C. M. Papa, F. N. Castellano and M. Abolhasani, *Advanced Functional Materials*, 2019, **29**, 1900712.
38. S.-M. Kang, B. Park, G. S. R. Raju, S. Baek, S. K. Hussain, C. H. Kwak, Y.-K. Han, J. S. Yu, S.-W. Kim and Y. S. Huh, *Chemical Engineering Journal*, 2020, **384**, 123316.
39. R. M. Maceiczky, L. Bezingue and A. J. deMello, *Reaction Chemistry & Engineering*,

- 2016, **1**, 261-271.
40. Y. Tang, H. Lu, L. Rao, Z. Li, X. Ding, C. Yan and B. Yu, *Materials*, 2018, **11**, 371.
 41. Z. Zhang, Y. Liu, C. Geng, S. Shi, X. Zhang, W. Bi and S. Xu, *Nanoscale*, 2019, **11**, 18790-18796.
 42. R. M. Maceiczky, K. Dümbgen, I. Lignos, L. Protesescu, M. V. Kovalenko and A. J. deMello, *Chemistry of Materials*, 2017, **29**, 8433-8439.
 43. I. Lignos, L. Protesescu, D. B. r. Emiroglu, R. Maceiczky, S. Schneider, M. V. Kovalenko and A. J. deMello, *Nano Letters*, 2018, **18**, 1246-1252.
 44. I. Lignos, V. Morad, Y. Shynkarenko, C. Bernasconi, R. M. Maceiczky, L. Protesescu, F. Bertolotti, S. Kumar, S. T. Ochsenein and N. Masciocchi, *ACS Nano*, 2018, **12**, 5504-5517.
 45. L. Bezing, R. M. Maceiczky, I. Lignos, M. V. Kovalenko and A. J. deMello, *ACS Applied Materials & Interfaces*, 2018, **10**, 18869-18878.
 46. F. Yang, *The European Physical Journal Applied Physics*, 2022, **97**.
 47. M. R. Karim, M. Balaban and H. Unlu, *Advances in Materials Science and Engineering*, 2019, **2019**, 3764395.
 48. X. Li, Y. Wu, S. Zhang, B. Cai, Y. Gu, J. Song and H. Zeng, *Advanced Functional Materials*, 2016, **26**, 2435-2445.
 49. Z. Wei, Y. Chen, P. Lin, Q. Yan, Y. Fan and Z. Cheng, *Journal of Materials Science*, 2019, **54**, 6841-6852.
 50. P. Lin, H. Chen, Z. Wei, Y. Lin, J. Lin, Y. Chen and Z. Cheng, *Science China Materials*, 2020, **63**, 1526-1536.
 51. C. K. Ng, H. Deng, H. Li, W. Yin, T. Alan and J. J. Jasieniak, *Journal of Materials Chemistry C*, 2021, **9**, 313-321.
 52. F. Zhang, H. Zhong, C. Chen, X.-g. Wu, X. Hu, H. Huang, J. Han, B. Zou and Y. Dong, *ACS Nano*, 2015, **9**, 4533-4542.
 53. Y. Zhang, T. D. Siegler, C. J. Thomas, M. K. Abney, T. Shah, A. De Gorostiza, R. M. Greene and B. A. Korgel, *Chemistry of Materials*, 2020, **32**, 5410-5423.
 54. P.-H. Haumesser, *Nucleation and growth of metals: from thin films to nanoparticles*,

Elsevier, ISTE Press, London, UK 2016.

55. A. A. Al-Tabbakh, N. Karatepe, A. B. Al-Zubaidi, A. Benchaabane and N. B. Mahmood, *International Journal of Energy Research*, 2019, **43**, 1903-1911.
56. E. Hanamura, in *Confined Electrons and Photons*, Springer, New York 1995, pp. 831-837.
57. Z. Fu, Y. Cui, S. Zhang, J. Chen, D. Yu, S. Zhang, L. Niu and J. Jiang, *Applied Physics Letters*, 2007, **90**, 263113.
58. F. Yang, *Physics Letters A*, 2021, **401**, 127346.
59. F. Yang, *Langmuir*, 2021, **37**, 3912-3921.
60. C. Fanelli, V. Cregan, F. Font and T. Myers, *International Journal of Heat and Mass Transfer*, 2021, **165**, 120643.
61. F. Yang, *Physical Chemistry Chemical Physics*, 2021, **23**, 3974-3982.
62. Y. P. Varshni, *Physica*, 1967, **34**, 149-154.
63. M. Ezzeldien, S. Al-Qaisi, Z. Alrowaili, M. Alzaid, E. Maskar, A. Es-Smaili, T. V. Vu and D. Rai, *Scientific Reports*, 2021, **11**, 1-12.
64. G. Mannino, I. Deretzis, E. Smecca, A. La Magna, A. Alberti, D. Ceratti and D. Cahen, *The Journal of Physical Chemistry Letters*, 2020, **11**, 2490-2496.